Microgravity Science and Technology (2021) 33: 5
https://doi.org/10.1007/s12217-020-09857-1

ORIGINAL ARTICLE

Steady thermocapillary droplet migration under thermal radiation with a uniform flux

Jia-Hao Gao[1,2] · Zuo-Bing Wu[1,2]

Received: 19 July 2020 / Accepted: 2 December 2020 / Published online: 7 January 2021
© Springer Nature B.V. 2021

Abstract

Thermocapillary migration of a droplet under thermal radiation with a uniform flux is numerically investigated and theoretically analyzed. By using the front-tracking method, it is observed that thermocapillary droplet migration at small Reynolds numbers and moderate Marangoni numbers reaches a steady process. The steady migration velocity decreases as Marangoni number increases. The time-evolution behavior of temperature fields in the steady migration process is found to be a quadratic function, in which the linear rise of the steady state temperatures with the relative time is a main characteristics. The quadratic function behavior of the temperature fields is further used to derive the steady energy equations. From the steady momentum and energy equations, an analytical result at small Reynolds number and zero Marangoni number is determined by using the method of matched asymptotic expansions. The steady migration velocity decreases as Reynolds number increases, which is in qualitatively agreement with the numerical result.

Keywords Thermocapillary · Droplet · Thermal radiation · Surface tension · Steady state

Introduction

In the microgravity environment, the migration of a droplet in a bulk liquid is caused by the non-uniform surface tension distribution along the interface between the two immiscible fluids and known as thermocapillary droplet migration. Such nonisothermal interfacial flow is very important in both the fundamental hydrodynamics and the industrial application such as production of pure materials (Ratke and Korekt 2000) and mass transfer in chemical engineering (Bassano and Castagnolo 2003). To generate the non-uniform surface tension, on one hand, a vertical temperature gradient field is added in the bulk liquid through providing the non-uniform temperature distribution along the interface. (Young et al. 1959) firstly studied thermocapillary migration of a droplet in a vertical temperature gradient field and obtained the droplet migration velocity in the limit case of zero Reynolds (Re) and Marangoni (Ma) numbers. Subramanian (1981) introduced the quasi-steady state assumption, extended the YGB's result to the small Ma numbers and obtained an asymptotic solution for the steady migration velocity. Since then, due to the effect of the vertical temperature gradient field in the bulk liquid, the thermocapillary droplet migration and its mechanism are understood very well in a series of theoretical analyses, numerical simulations, and experimental investigations (Subramanian et al. 2001; Yin et al. 2009; Zhang et al. 2018; Alhendal et al. 2018).

On the other hand, the thermal radiation to the droplet surface is another method to generate the non-uniform surface tension through providing the non-uniform temperature distribution along the interface. Oliver and Dewitt (1988) firstly analyzed the thermocapillary droplet migration under the thermal radiation with a uniform flux at the zero limits of Re and Ma numbers and obtained the droplet migration velocity. Rednikov and Ryzzantsev (1989) independently derived the same results and determined the deformation of the droplet. Rybalko et al. (2004) experimentally investigated the directed motion of an oil droplet floating in an aqueous solution guided by a laser beam focused at the oil-water interface, where exists the variation of surface tension due to the thermal gradient at the interface.

✉ Zuo-Bing Wu
wuzb@lnm.imech.ac.cn

1 LNM, Institute of Mechanics, Chinese Academy of Sciences, Beijing, 100190, China

2 School of Engineering Science, University of Chinese Academy of Sciences, Beijing, 100049, China

Baroud et al. (2007) experimentally and theoretically illustrated the effects of laser-driven localized thermocapillary stresses on microactuation of water droplets in oil. Vincent and Delville (2012) experimentally investigated the thermocapillary migration induced by local laser heating of the advancing front of a growing droplet confined in a microfluidic channel. Lopez et al. (2013) and Rendondo et al. (2014) experimentally observed thermocapillary migration of a droplet caused by laser beam heating due to the absorption of laser radiation by making a strongly nonhomogeneous distribution of temperature inside the droplet as well as at its surface. Ryazantsev et al. (2017) reported thermo- and soluto-capillary migration of passive and active droplets with a laser beam under various forms of illumination. Zhang et al. (2018) numerically studied the spontaneous droplet migration under thermal radiation in a large range of Re numbers and investigated effects of the physical parameters of two-phase fluids on the steady migration velocity. Wu (2018) theoretically analyzed steady thermocapillary migration of a droplet at large Ma numbers under a combination of a vertical temperature gradient and a uniform radiation energy source. However, some interesting topics on thermocapillary droplet migration under thermal radiation, such as effects of Ma number on the terminal velocity, time evolution of temperature distributions in the steady state migration processes, remain to be studied with respect to its physical mechanism.

In this paper, we firstly numerically investigate effects of Ma number on thermocapillary droplet migration under thermal radiation with a uniform flux at small Re numbers. And then, we extend the OD's analytical result to the case of small Re numbers and determine the steady migration velocity. Section "Governing equations" describes the model and formulation of thermocapillary droplet migration under the thermal radiation. The numerical results of the thermocapillary droplet migration in a large range of Ma numbers are analyzed in "Numerical simulation of thermocapillary droplet migration at small Re and moderate Ma numbers". The analytical result of the steady thermocapillary migration of a droplet in the limiting case of zero Ma number in relation to small Re number is determined and compared with the corresponding numerical one in "Theoretical analysis of thermocapillary droplet migration at small Re and zero Ma numbers". Finally, in "Conclusion and discussion", some conclusions and discussions are given.

Governing equations

Consider a single droplet with a radius R_0 placed in a continuous-phase fluid of unbounded extend under thermal radiation with a uniform flux q. Gravity and deformation of the droplet shape are ignored. The droplet surface and the continuous-phase fluid are assumed as a gray body and transparent to the radiation, respectively. The droplet moves up due to the non-uniform surface tension $\sigma = \sigma_0 + \sigma_T(\bar{T} - T_0)$, where σ_0 and σ_T are the surface tension coefficient at the undisturbed temperature T_0 and the changing rate of the interfacial tension between the droplet and the continuous-phase fluid with temperature $\bar{T}$, respectively. The continuity, momentum and energy equations for the continuous-phase fluid and the droplet in a laboratory coordinate system $(\bar{r}, \bar{z})$ are written as

$$\begin{aligned}
&\frac{\partial \rho_i}{\partial t} + \bar{\nabla} \cdot (\rho_i \bar{\mathbf{v}}_i) = 0,\\
&\frac{\partial \rho_i}{\bar{\mathbf{v}}_i} \partial t + \bar{\nabla} \cdot (\rho_i \bar{\mathbf{v}}_i \bar{\mathbf{v}}_i) = -\bar{\nabla} \bar{p}_i + \bar{\nabla} \cdot \left[\mu_i (\bar{\nabla} \bar{\mathbf{v}}_i + \bar{\nabla}^T \bar{\mathbf{v}}_i) \right],\\
&\frac{\partial \bar{T}_i}{\partial t} + \bar{\nabla} \cdot (\bar{\mathbf{v}}_i \bar{T}_i) = \frac{\kappa_i}{k_i} \bar{\nabla} \cdot (k_i \bar{\nabla} \bar{T}_i),
\end{aligned} \tag{1}$$

where the symbols $\bar{\mathbf{v}}_i$, $\bar{p}_i$, $\bar{T}_i$ represent the velocity, pressure and temperature, respectively. The direction of the incident irradiation is antiparallel to the $\bar{z}$-axis. ρ_i, μ_i, k_i and κ_i represent the density, the dynamical viscosity, the thermal conductivity and the thermal diffusivity, respectively. Symbols with subscript 1 and 2 denote physical variables and coefficients of the continuous-phase fluid and the droplet, respectively. The solutions of Eq. 1 have to satisfy the boundary conditions at infinity

$$\bar{\mathbf{v}}_1 \to 0, \quad \bar{p}_1 \to p_\infty, \quad \bar{T}_1 \to T_0 \tag{2}$$

and at the interface $\bar{\mathbf{r}}_b$ of the two-phase fluids

$$\begin{aligned}
&\bar{\mathbf{v}}_1(\bar{\mathbf{r}}_b, t) = \bar{\mathbf{v}}_2(\bar{\mathbf{r}}_b, t),\\
&\mathbf{n} \cdot \bar{\Pi}_1 \cdot \mathbf{n} - \mathbf{n} \cdot \bar{\Pi}_2 \cdot \mathbf{n} = 2\sigma H,\\
&\mathbf{n} \cdot \bar{\Pi}_1 \cdot \mathbf{s} - \mathbf{n} \cdot \bar{\Pi}_2 \cdot \mathbf{s} = -\bar{\nabla}_s \sigma \cdot \mathbf{s},\\
&\bar{T}_1(\bar{\mathbf{r}}_b, t) = \bar{T}_2(\bar{\mathbf{r}}_b, t),\\
&k_1 \frac{\partial \bar{T}_1}{\partial n}(\bar{\mathbf{r}}_b, t) - q\mathbf{i}_{\bar{z}} \cdot \mathbf{n} = k_2 \frac{\partial \bar{T}_2}{\partial n}(\bar{\mathbf{r}}_b, t),
\end{aligned} \tag{3}$$

where $\bar{\Pi}_1$ and $\bar{\Pi}_2$ is the stress tensors of the two-phase fluids. $\mathbf{n}$ and $\mathbf{s}$ are the unit vectors normal and tangent to the interface, respectively. $\mathbf{i}_{\bar{z}}$ is a unit vector of the $\bar{z}$-axis. $\bar{\nabla}_s (= \bar{\nabla} - \mathbf{n}\frac{\partial}{\partial n})$ is the surface gradient operator. H is the curvature of the interface.

In the modeling assumptions, both fluids are immiscible, and the physical properties are constant. The droplet keeps a spherical axisymmetric shape ($H = 1/R_0$). The equations of states for density, viscosity, heat conduction and heat diffusivity are written as follows

$$\frac{d\rho_i}{dt} = \frac{d\mu_i}{dt} = \frac{dk_i}{dt} = \frac{d\kappa_i}{dt} = 0. \tag{4}$$

By taking the radius of the droplet R_0, the velocity $v_0 = -\sigma_T q R_0 / k_1 \mu_1$ and $q R_0 / k_1$ as the reference quantities to

make coordinates, velocity and temperature dimensionless, Eq. 1 is rewritten as

$$\begin{aligned}
&\bar{\nabla}\cdot\bar{\mathbf{v}}_i = 0,\\
&\rho_i\frac{\partial\bar{\mathbf{v}}_i}{\partial t} + \rho_i\bar{\mathbf{v}}_i\cdot\bar{\nabla}\bar{\mathbf{v}}_i = -\bar{\nabla}\bar{p}_i + \frac{1}{Re}\bar{\nabla}\cdot\left[\mu_i(\bar{\nabla}\bar{\mathbf{v}}_i + \bar{\nabla}\bar{\mathbf{v}}_i^T)\right],\\
&\frac{\partial\bar{T}_i}{\partial t} + \bar{\mathbf{v}}_i\cdot\bar{\nabla}\bar{T}_i = \frac{\kappa_i/k_i}{Ma}\bar{\nabla}\cdot(k_i\bar{\nabla}\bar{T}_i).
\end{aligned} \tag{5}$$

The physical coefficients ρ_i, μ_i, k_i and κ_i are nondimensionlized by the quantities of continuous-phase fluid. Re, Ma and Prandtl (Pr) numbers are respectively defined as

$$Re = \frac{\rho_1 v_0 R_0}{\mu_1}, \quad Ma = \frac{v_0 R_0}{\kappa_1}, \quad \text{and} \quad Pr = \frac{Ma}{Re} = \frac{\mu_1}{\rho_1\kappa_1}. \tag{6}$$

The solutions of Eq. 5 have to satisfy the boundary conditions at infinity

$$\bar{\mathbf{v}}_1 \to 0, \quad \bar{p}_1 \to 0, \quad \bar{T}_1 \to 0 \tag{7}$$

and at the interface $\bar{\mathbf{r}}_b$ of the two-phase fluids

$$\begin{aligned}
&\bar{\mathbf{v}}_1(\bar{\mathbf{r}}_b, t) = \bar{\mathbf{v}}_2(\bar{\mathbf{r}}_b, t),\\
&\mathbf{n}\cdot\bar{\Pi}_1\cdot\mathbf{n} - \mathbf{n}\cdot\bar{\Pi}_2\cdot\mathbf{n} = 2\sigma H,\\
&\mathbf{n}\cdot\bar{\Pi}_1\cdot\mathbf{s} - \mathbf{n}\cdot\bar{\Pi}_2\cdot\mathbf{s} = -\frac{\partial\sigma}{\partial s},\\
&\bar{T}_1(\bar{\mathbf{r}}_b, t) = \bar{T}_2(\bar{\mathbf{r}}_b, t),\\
&\frac{\partial\bar{T}_1}{\partial n}(\bar{\mathbf{r}}_b, t) + \mathbf{i}_{\bar{z}}\cdot\mathbf{n} = k_2\frac{\partial\bar{T}_2}{\partial n}(\bar{\mathbf{r}}_b, t),
\end{aligned} \tag{8}$$

where $\sigma = \frac{1}{Ca} - \bar{T}_1$. $Ca(= \frac{v_0\mu}{\sigma_0})$ is the Capillary number.

Numerical simulation of thermocapillary droplet migration at small Re and moderate Ma numbers

Models and numerical methods

As shown schematically in Fig. 1a, the symmetric axis of the container is taken as the $\bar{z}$-axis. An axisymmetric droplet is placed initially at the center of coordinates and then moved along the $\bar{z}$-axis under the thermal radiation with a uniform flux. The continuous, momentum and energy equations with the surface tension force $\delta\mathbf{F}_\sigma$ and the radiative heat flux δQ in a cylindrical coordinate system $(\bar{r}, \bar{z})$ are written as

$$\begin{aligned}
&\bar{\nabla}\cdot\bar{\mathbf{v}}_i = 0,\\
&\frac{\partial(\rho_i\bar{\mathbf{v}}_i)}{\partial t} + \bar{\nabla}\cdot(\rho_i\bar{\mathbf{v}}_i\bar{\mathbf{v}}_i) = -\bar{\nabla}\bar{p}_i + \frac{1}{Re}\bar{\nabla}\\
&\quad\cdot\left[\mu_i(\bar{\nabla}\bar{\mathbf{v}}_i + \bar{\nabla}\bar{\mathbf{v}}_i^T)\right] + \frac{1}{Re}\delta\mathbf{F}_\sigma,\\
&\frac{\partial\bar{T}_i}{\partial t} + \bar{\mathbf{v}}_i\cdot\bar{\nabla}\bar{T}_i = \frac{\kappa_i/k_i}{Ma}\bar{\nabla}\cdot(k_i\bar{\nabla}\bar{T}_i) + \frac{\kappa_i/k_i}{Ma}\delta Q,
\end{aligned} \tag{9}$$

where

$$\begin{aligned}
\delta\mathbf{F}_\sigma &= \frac{\int_{\Delta s_{AB}}\left(-2\sigma H\mathbf{n} + \frac{\partial\sigma}{\partial s}\mathbf{s}\right)2\pi r\delta^2(\bar{\mathbf{r}} - \bar{\mathbf{r}}_b)ds}{2\pi r_c\Delta r\Delta z}\\
&= \frac{[(\sigma r\mathbf{s})_B - (\sigma r\mathbf{s})_A] - \sigma_c\Delta s_{AB}\mathbf{i}_{\bar{r}}}{r_c\Delta\bar{r}\Delta\bar{z}}
\end{aligned} \tag{10}$$

and

$$\delta Q = \frac{\int_{\Delta s_{AB}}\mathbf{i}_{\bar{z}}\cdot\mathbf{n}2\pi r\delta^2(\bar{\mathbf{r}} - \bar{\mathbf{r}}_b)ds}{2\pi r_c\Delta r\Delta z} = \frac{sin^2\frac{\theta_B}{2} - sin^2\frac{\theta_A}{2}}{r_c\Delta\bar{r}\Delta\bar{z}}. \tag{11}$$

δ^2 is a two-dimensional function constructed by the repeated multiplication of the one-dimensional Dirac delta function. $\bar{\mathbf{r}}$ and $\bar{\mathbf{r}}_b$ are the points in the computational domain and on the interface, respectively. Δs_{AB} is a short front element on the interface. r_c is the radius of the cross section at the center c of Δs_{AB}. θ is the angle coordinate of the interface s. $\mathbf{i}_{\bar{r}}$ is a unit vector of the $\bar{r}$-axis. The solutions of Eq. 9 satisfy the initial conditions of the computational domain $\bar{r} \in [0, r_1]$ and $\bar{z} \in [z_1, z_2]$

$$\begin{aligned}
&\bar{\mathbf{v}}_i = 0,\\
&\bar{T}_i = 0
\end{aligned} \tag{12}$$

and the boundary conditions at the top and bottom walls ($\bar{z} = z_1$ and $\bar{z} = z_2$), on the symmetric central axis ($\bar{r} = 0$) and at the right wall ($\bar{r} = r_1$)

$$\begin{array}{lll}
\bar{v}_{r,1}(\bar{r}, z_1) = \bar{v}_{r,1}(\bar{r}, z_2) = 0, & \frac{\partial\bar{v}_{z,1}}{\partial\bar{z}}(\bar{r}, z_1) = \frac{\partial\bar{v}_{z,1}}{\partial\bar{z}}(\bar{r}, z_2) = 1, & \frac{\partial\bar{T}_1}{\partial\bar{z}}(\bar{r}, z_1) = \frac{\partial\bar{T}_1}{\partial\bar{z}}(\bar{r}, z_2) = 1,\\
\bar{v}_{r,i}(0, \bar{z}) = 0, & \frac{\partial\bar{v}_{z,i}}{\partial\bar{r}}(0, \bar{z}) = 1, & \frac{\partial\bar{T}_i}{\partial\bar{r}}(0, \bar{z}) = 1,\\
\bar{v}_{r,1}(r_1, \bar{z}) = 0, & \frac{\partial\bar{v}_{z,1}}{\partial\bar{r}}(r_1, \bar{z}) = 1, & \bar{T}_1(r_1, \bar{z}) = 0.
\end{array} \tag{13}$$

In the following computation, we apply a regular staggered Marker-And-Cell grid in the computational domain, a second-order central difference scheme for the spatial variables and an explicit predictor-corrector second-order scheme for time integration of the above momentum and energy equations. Since both fluids are assumed immiscible, all physical coefficients are discontinuous across the interface. The interface is captured and updated by the front-tracking method (Tryggvason et al. 2001), so all discontinuous physical coefficients across the interface are treated as continuous. The conversion of the physical quantities between the interface nodes $(\bar{r}_p, \bar{z}_p)$ and the grid points

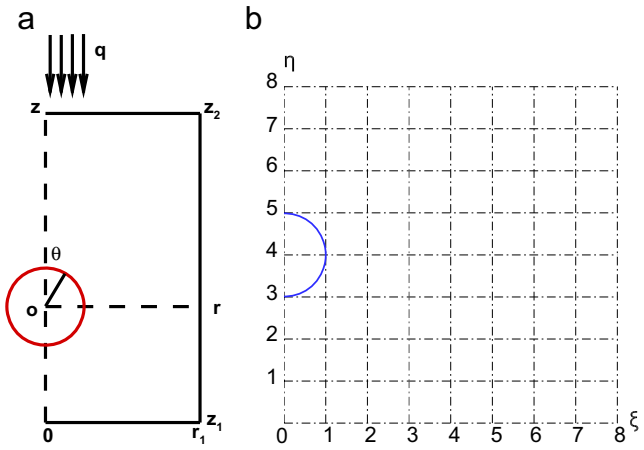

Fig. 1 **a** A schematic of the droplet migration system under the thermal radiation with a uniform flux in a laboratory coordinate system; **b** A mesh $(\xi, \eta) \in \{[0, 8], [0, 8]\}$ fixed at the reference frame moving with the droplet to recode the time evolution of the steady state temperature fields

$(i\Delta\bar{r}, j\Delta\bar{z})$ is treated with the Peskin's weighting function (Peskin 1977)

$$w_{ij}(\bar{\mathbf{r}}_p) = d(\bar{r}_p - i\Delta\bar{r})d(\bar{z}_p - j\Delta\bar{z}), \tag{14}$$

$$d(r) = \begin{cases} (1/4h)[1 + \cos(\pi r/2h)], & |r| < 2h, \\ 0, & |r| \geq 2h, \end{cases} \tag{15}$$

where h is the grid spacing in r. To calculate the surface tension force $\delta\mathbf{F}_\sigma$, the temperature on the interface is determined by interpolating values on the grid points. The tangent vector $\mathbf{s}$ is computed from a Lagrangian interpolation polynomial fitting through four interface nodes. The surface tension force $\delta\mathbf{F}_\sigma$ and the radiative heat flux δQ on the interface are distributed to the grid points by means of the weighting function Eq. 14, respectively. More details of the numerical methods can be found in (Tryggvason et al. 2001; Wu and Hu 2012).

Numerical results

To validate the methods described above, we carry out several benchmark testing. The parameters $\rho_2 = \mu_2 = k_2 = \kappa_2 = 0.8$, Pr=1 and Ca=0.1 are fixed, except for some cases declared. The time step is chosen as $O(10^{-6}) \sim O(10^{-7})$. First of all, to examine the impact of the computational domain ($\{\bar{r}, \bar{z}\} \in \{[0, r_1], [-4, 8]\}$) on numerical results, we choose $r_1 = 6, 8, 10, 12$ and perform calculations for the droplet migration based on the grid refinement for 32 grid points per droplet radius at Re = Ma = 0.01. The time evolution of the droplet migration velocity is calculated and plotted in Fig. 2a. The terminal migration velocity curve with a small fluctuation (about 1%) seems

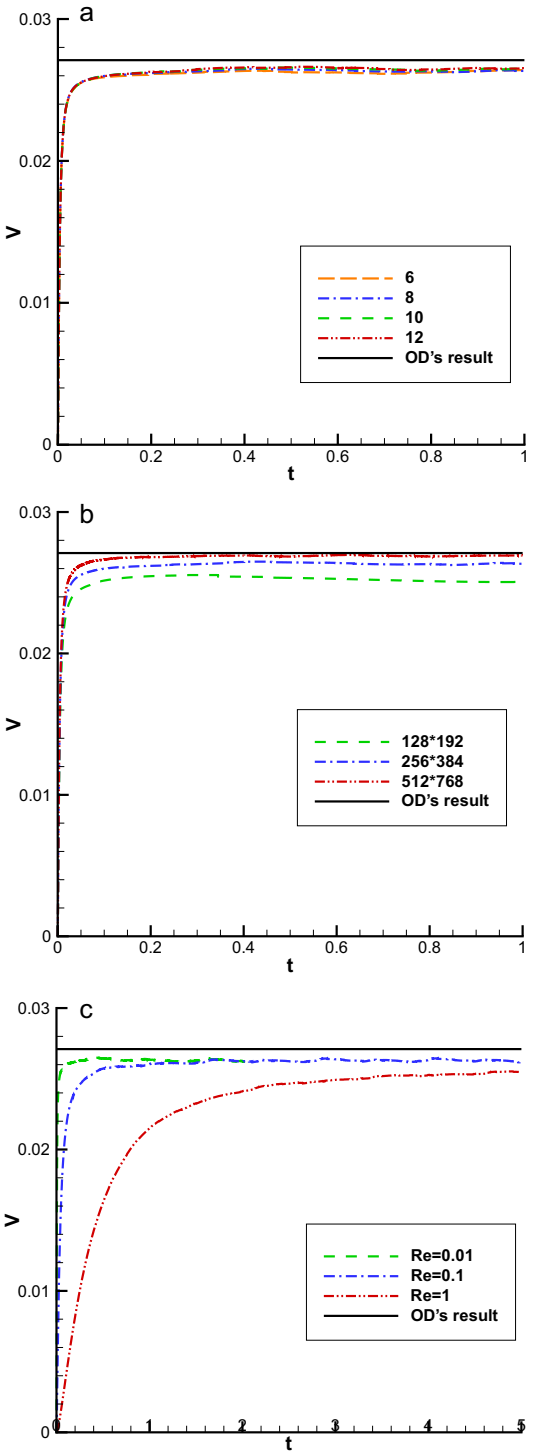

Fig. 2 Droplet migration velocity versus time at Pr=1, Ca=0.1 and $\alpha = \beta = \gamma = \lambda = 0.8$ for **a** four computational domains $\{\bar{r}, \bar{z}\} \in \{[0, r_1], [-4, 8]\}$ ($r_1 = 6, 8, 10, 12$) with the fixed grid resolution for 32 grid points per droplet radius at Re(Ma)=0.01; **b** three grid resolutions 128 × 192, 256 × 384 and 512 × 576 in the fixed computational domain $\{\bar{r}, \bar{z}\} \in \{[0, 8], [-4, 8]\}$ at Re(Ma)=0.01; **c** three groups of Re(Ma) = (0.01, 0.1, 1) at the fixed computational domain $\{\bar{r}, \bar{z}\} \in \{[0, 8], [-4, 8]\}$ and the fixed grid resolution 256 × 384. The OD's analytical result at zero limits of Re and Ma numbers is also provided for comparison

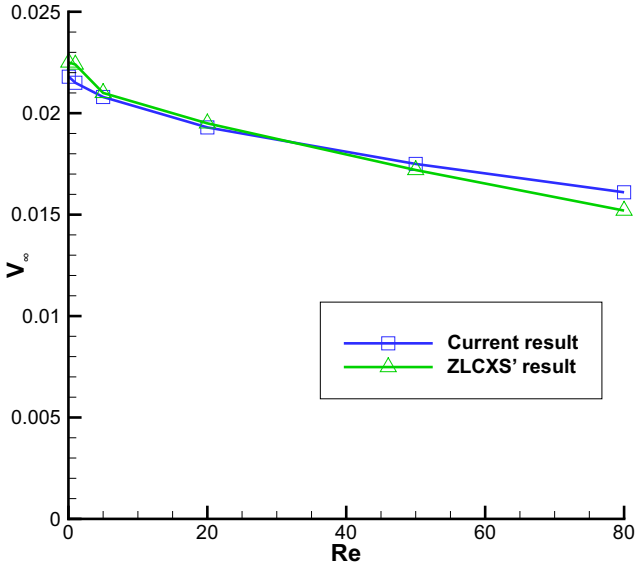

Fig. 3 Comparison of the steady droplet migration velocity V_∞ versus Re number at the fixed computational domain $\{\bar{r}, \bar{z}\} \in \{[0, 8], [-4, 8]\}$ and the fixed grid resolution 256 × 384 with the ZLCXS' numerical result for Pr=1, Ca=0.1 and $\alpha = \beta = \gamma = \lambda = 1$ (Zhang et al. 2018)

to converge when $r_1 \geq 6$. The derivation of the converged terminal migration velocity from the OD's analytical result ($V_\infty = 0.027$) is very small (about 3%). Secondly, to check the sensitivity of numerical results to grid refinements, we complete calculations for the droplet migration in the computational domain $\{\bar{r}, \bar{z}\} \in \{[0, 8], [-4, 8]\}$ at Re = Ma =0.01. Based on 128 × 192, 256 × 384 and 512 × 576 grid points, i.e., 16, 32 and 48 grid points per droplet radius, the time evolution of the droplet migration velocity is calculated and plotted in Fig. 2b. The terminal migration velocity curve seems to converge towards the OD's analytical result when the grid becomes finer. The difference in the migration velocities computed with 32 and 48 grid points per droplet radius is very small (about 2%). And then, we compare the computational result with the OD's analytical one at the zero limits of Re and Ma numbers (Oliver and Dewitt 1988). As shown in Fig. 2c, the migration velocities of the droplet with the grid resolution for 32 grid points per droplet radius at small Re(Ma) numbers (0.01, 0.1 and 1) exhibit a convergent approximation to the OD's analytical result with an error (about 3%) as the Re(Ma) number decreases. Finally, to validate the code, we compare the current numerical results with the ZLCXS' ones at $\rho_2 = \mu_2 = k_2 = \kappa_2 = 1$ in a range of Re numbers (Zhang et al. 2018). In Fig. 3, it is observed that both the steady migration velocities are very close together and have the same trends. In the following calculations, we fix the computational domain as $\{\bar{r}, \bar{z}\} \in \{[0, 8], [-4, 8]\}$, the grid resolution as 32 grid points per droplet radius and the time step as $O(10^{-4}) \sim O(10^{-6})$.

Fig. 4a displays the time evolution of the droplet migration velocity at Ma=0.5, 5, 10, 50, 100, 200 and Pr=50. For each Ma case, the droplet migration velocity firstly monotonically increases as time increases, and then approaches to a steady value. The transient migration process to reach the steady state is longer as Ma number increases. This phenomenon accords with the principle that Ma number as the dimensionless thermal diffusion time scale is the controlling parameter of the thermocapillary droplet migration to reach the terminal state (Wu 2017). As given in Fig. 4b, the steady migration velocity decreases

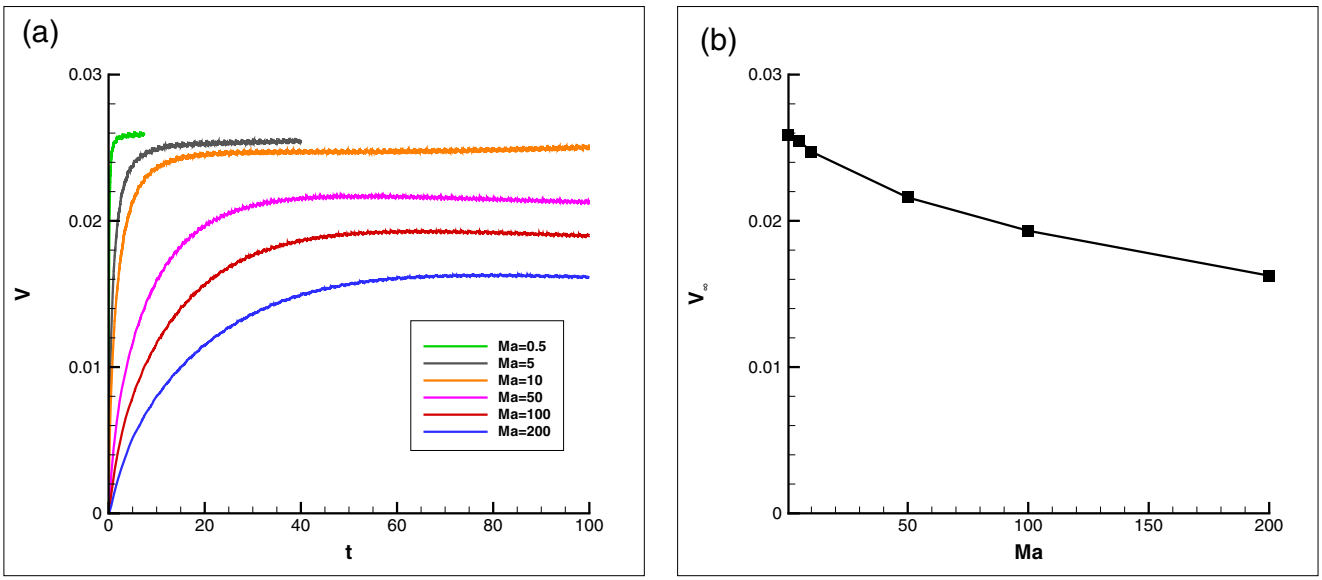

Fig. 4 **a** Time evolution of droplet migration velocity for Ma=0.5, 5, 10, 50, 100 and 200 at Pr=50 and Ca=0.1; **b** Steady migration velocity V_∞ versus Ma number

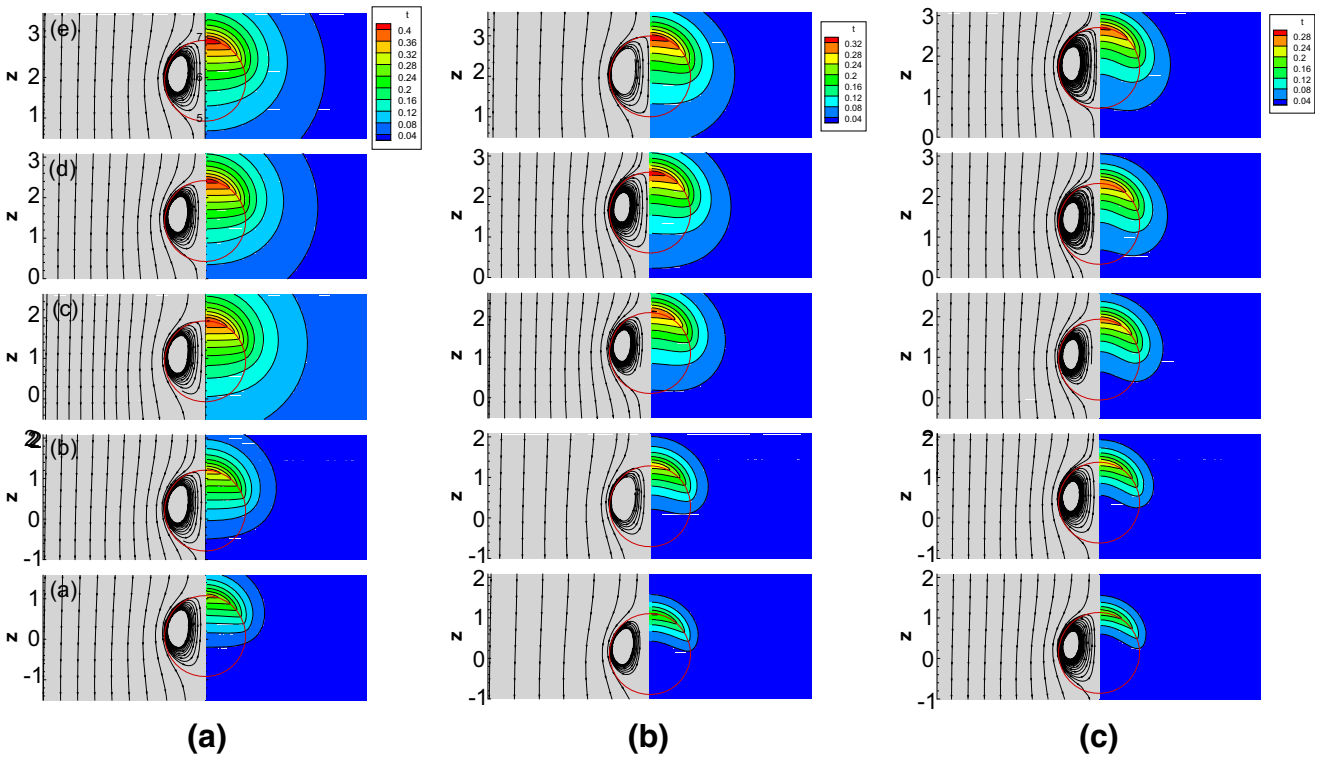

Fig. 5 Streamlines in the reference frame moving with the droplet and isotherms in a laboratory coordinate frame **a** at time 5, 10, 40, 60, 80 for Ma=10, **b** at time 10, 20, 60, 80, 100 for Ma= 50 and **c** at time 15, 30, 60, 80, 100 for Ma=100

as Ma number increases. Figure 5a displays the time evolution of the streamlines in a reference frame moving with the droplet and isotherms in a laboratory coordinate system at Ma=10. Since the radiative heat flux passing through the interface is a cosine function, a temperature gradient along the interface appears under the thermal radiation. The interfacial temperature gradient leads to the non-uniform surface tension distribution. As a result, the net force generated by the surface tension drives the droplet to move up. Meanwhile, the surface tension also induces viscous stresses in both fluids near the interface and generate flow patterns outside and inside the droplet. The external flow around the droplet does not separate from the droplet surface. Two vortices appeared in the droplet are symmetric about the vertical diameter. The vortex centers hardly move in the droplet and the velocity fields are almost kept during the droplet migration process. The velocity fields in the steady migration process are similar to those in thermocapillary droplet migration with a vertical temperature gradient. Moreover, the upper surface of the droplet absorbs the radiative thermal energy and transfers it into two-phase fluids. As the time increases, the isotherms propagate far away from the interface. The internal and external isotherms display horizontal and arc, respectively. The isotherms connect at the surface of the droplet and show a mushroom-cap shape. The temperature fields in the steady migration process are different from those in thermocapillary droplet migration with the vertical temperature gradient. At Ma=10, the heat convection is slightly stronger than the heat conduction in the energy redistribution. To further analyze features of the temperature fields when the droplet moves in the steady state process, we take a 8×8 mesh fixed at the reference frame moving with the droplet as shown in Fig. 1b and depict the time evolution of steady state temperature at each point of the mesh. In Fig. 6a and b. the temperature rise from the steady state at each point $(\xi, \eta) \in \{[0, 7], [0, 8]\}$ is a quadratic function of relative time to the starting time $t_s = 40$ of the steady state, i.e., $\Delta\bar{T}_i(\mathbf{r}) = \bar{T}_i(\bar{\mathbf{r}}, t) - T_i(\mathbf{r}) = G_1(\mathbf{r})(t - t_s) + G_2(\mathbf{r})(t - t_s)^2$, where $T_i(\mathbf{r})$ is the steady state temperature when $t = t_s$. The functions G_1 and G_2, which are distribution functions of the position $\mathbf{r}$ in the reference frame moving with the droplet, depict the linear growth and the nonlinear supplement of the steady sate temperature with the relative time, respectively. Based on the data $(\Delta\bar{T}_i(\mathbf{r}), \Delta t = t - t_s)$ at each point, G_1 and G_2 are estimated by the least square polynomial fitting algorithm and given in the figure legends. In general, the function G_2 is two orders of magnitude lower than G_1. Within the time range of steady state evolution $[t - t_s = O(10)]$, the nonlinear term $G_2(t - t_s)^2$ is one order of magnitude lower than the linear term $G_1(t - t_s)$. So, the linear rise of the

steady state temperature with the relative time is a main characteristics in the steady droplet migration process. In the 72 reference points except for the 9 right boundary ones, the farther away from the droplet surface, the smaller the function G_1. Henceforth, the time evolution of steady state temperature for the points $(\xi, \eta) \in \{[4, 7], [0, 8]\})$ far from the droplet is omitted.

Figure 5b displays the time evolution of the streamlines in a reference frame moving with the droplet and isotherms in a laboratory coordinate system at Ma=50, respectively. At the moderate Ma number, the effect of the heat convection is stronger than that of the heat conduction. In the initial migration process, the thermal energy near the top surface of the droplet is hardly re-distributed into a large area through the heat conduction, but mainly gathers near the top surface of the droplet. In the droplet, the isotherms are bend due to the heat convection. When the droplet enters the steady state migration process, the isotherms propagate far away from the interface with the same shape. The time evolution of steady state temperature at each point of the mesh $(\xi, \eta) \in \{[0, 3], [0, 8]\})$ near the droplet starting from $t_s = 60$ is shown in Fig. 6c. For the 36 reference points, within the time range of steady state evolution $[t - t_s = O(10)]$, the nonlinear supplement $G_2(t - t_s)^2$ is one or more orders of magnitude lower than the linear term $G_1(t-t_s)$. Thus, the linear rise of the steady state temperature with the relative time is a main characteristics in the steady droplet migration process.

Figure 5c displays the time evolution of the streamlines in a reference frame moving with the droplet and isotherms in a laboratory coordinate system at Ma=100, respectively. At the moderate Ma number, the heat convection makes a main role in the energy redistribution. In the initial migration process, the thermal energy near the top surface of the droplet mainly gathers near the top surface of the droplet. In the droplet, the isotherms become more curved due to the stronger heat convection. The isotherms connected at

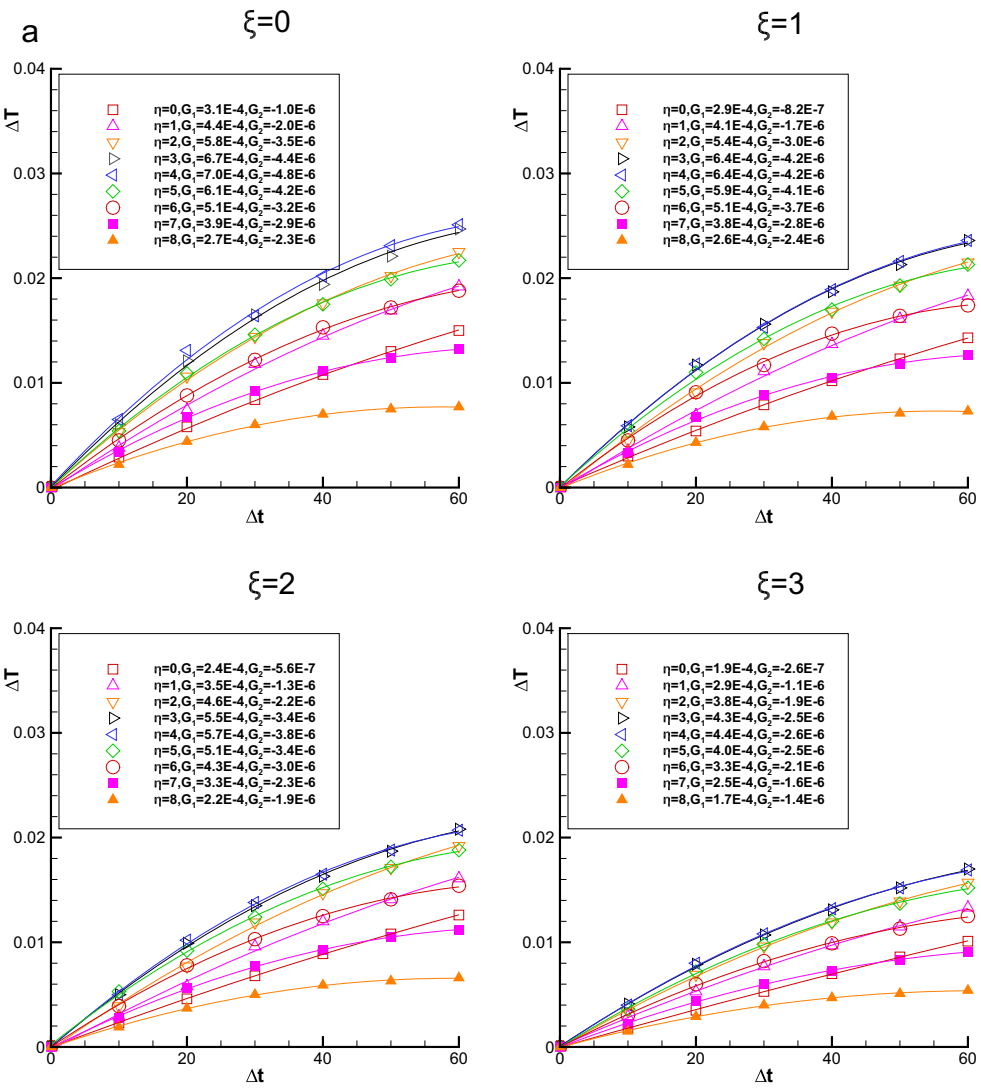

Fig. 6 Local temperature rise $\Delta\bar{T}_i$ with the relative time Δt in the steady migration process $(t \geq t_s)$ at each point of the mesh (a) $(\xi, \eta) \in \{[0, 3], [0, 8]\})$ for Ma=10 and $t_s = 40$; (b) $(\xi, \eta) \in \{[4, 7], [0, 8]\})$ for Ma=10 and $t_s = 40$; (c) $(\xi, \eta) \in \{[0, 3], [0, 8]\})$ for Ma=50 and $t_s = 60$ (d) $(\xi, \eta) \in \{[0, 3], [0, 8]\})$ for Ma=100 and $t_s = 60$. Solid lines described by a quadratic function with G_1 and G_2 are the least square polynomial fits of the points $(\Delta\bar{T}_i, \Delta t)$

Fig. 6 (continued)

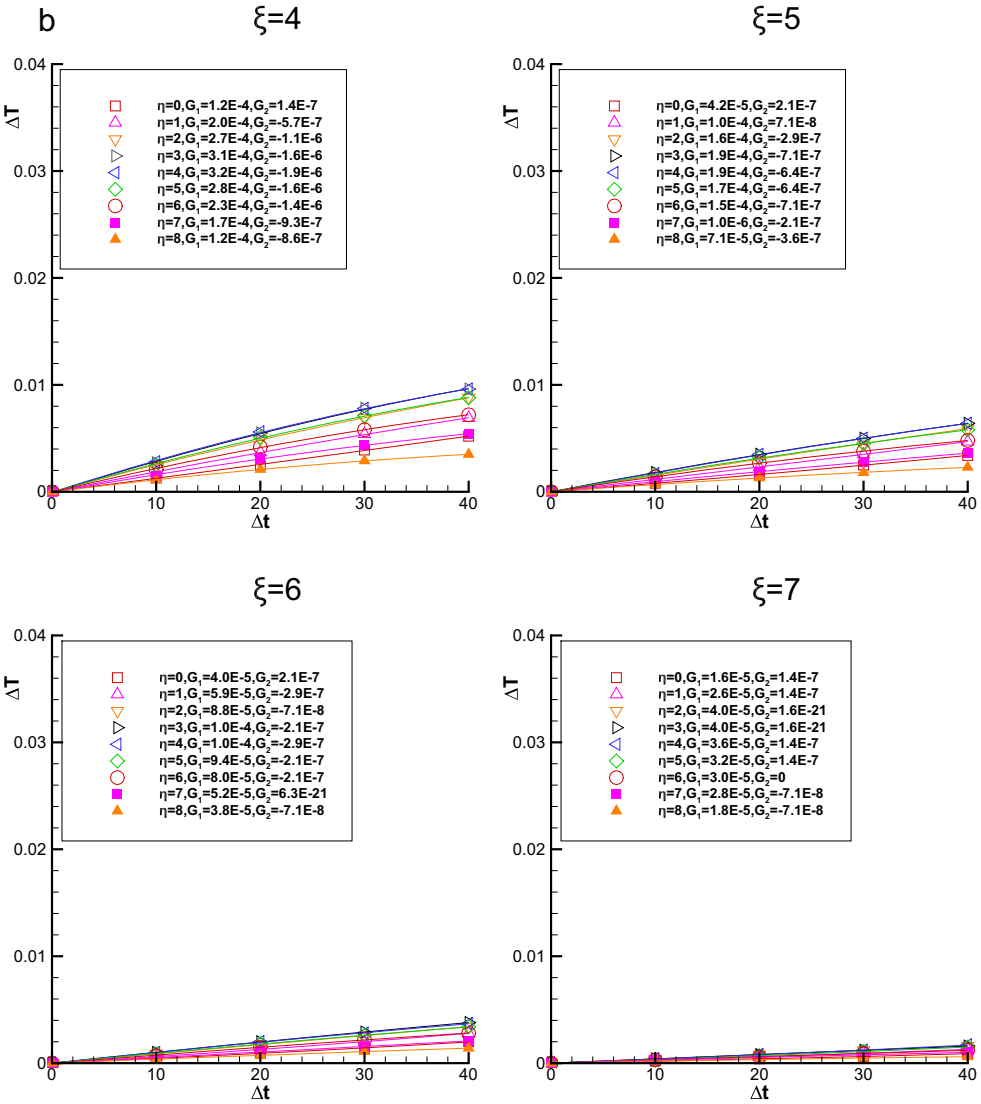

the surface of the droplet show an umbrella shape. When the droplet enters the steady state migration process, the isotherms keep the similar shape to propagate far away from the interface. In a similar way, the nonlinear supplement $G_2(t-t_s)^2$ is one or more orders of magnitude lower than the linear term $G_1(t-t_s)$. Therefore, we can conclude that within the time range of steady state evolution, the linear rise of the steady state temperature with the relative time is a main characteristics in the steady droplet migration process.

Theoretical analysis of thermocapillary droplet migration at small Re and zero Ma numbers

The droplet reaches a stable state with a constant migration velocity after an unsteady thermocapillary migration process, which inspires to introduce the quasi-steady state assumption and analyze features of the steady temperature fields. By using the coordinate and variable transformations from the laboratory coordinate system $(\bar{r},\bar{z})$ to a coordinate system (r,z) moving with the droplet, the steady continuity, momentum and energy equations are respectively derived from Eq. 5 in the Appendix and written as follows

$$\begin{aligned}&\nabla\cdot\mathbf{v}_i=0,\\&\rho_i\mathbf{v}_i\cdot\nabla\mathbf{v}_i=-\nabla p_i+\tfrac{\mu_i}{Re}\Delta\mathbf{v}_i,\\&G_1+\mathbf{v}_i\cdot\nabla T_i=\tfrac{\kappa_i}{Ma}\Delta T_i.\end{aligned}\tag{16}$$

At small Re and zero Ma numbers, Eq. 16 is rewritten in a spherical coordinate system (r,θ)

$$\begin{aligned}&\frac{\rho_i}{r^2}\frac{\partial(\psi_i,E^2\psi_i)}{\partial(r,\cos\theta)}+\frac{2\rho_i}{r^2}E^2\psi_iL\psi_i=\frac{\mu_i}{Re}E^4\psi_i,\\&\Delta T_i=0,\end{aligned}\tag{17}$$

Fig. 6 (continued)

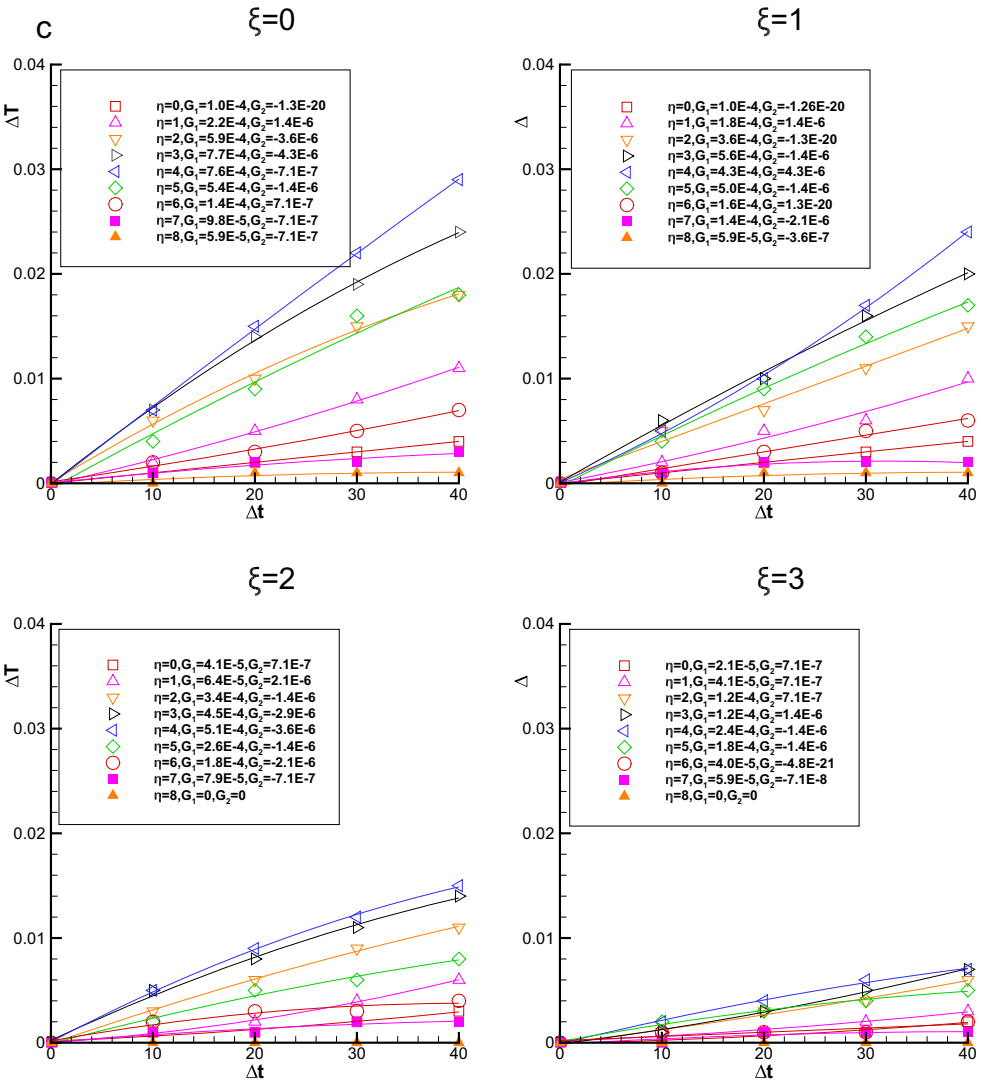

where

$$E^2 = \frac{\partial^2}{\partial r^2} + \frac{\sin^2\theta}{r^2}\frac{\partial^2}{\partial(\cos\theta)^2}, \tag{18}$$

$$L = \frac{\cos\theta}{\sin^2\theta}\frac{\partial}{\partial r} + \frac{1}{r}\frac{\partial}{\partial\cos\theta} \tag{19}$$

and ψ_i is the stream functions of the continuous fluid and the droplet. At the place far from the droplet, the velocity and temperature of the continuous fluid should satisfy

$$\begin{aligned} &\mathbf{v}_1(r\to\infty,\theta)\to(-V_\infty\cos\theta, V_\infty\sin\theta),\\ &T_1(r\to\infty,\theta)\to 0. \end{aligned} \tag{20}$$

At the droplet surface, the velocities inside and outside the droplet must meet the continuous and impermeable conditions described below

$$\begin{aligned} &v_{r,1}(1,\theta) = v_{r,2}(1,\theta) = 0,\\ &v_{\theta,1}(1,\theta) = v_{\theta,2}(1,\theta). \end{aligned} \tag{21}$$

Meanwhile, the temperatures and the heat fluxes inside and outside the droplet must be continuous and in balance with the thermal radiation as given below, respectively

$$T_1(1,\theta) = T_2(1,\theta) \tag{22}$$

and

$$\begin{aligned} &\frac{\partial T_1}{\partial r}(1,\theta) + \cos\theta = k_2\frac{\partial T_2}{\partial r}(1,\theta), \quad \theta\in[0,\pi/2],\\ &\frac{\partial T_1}{\partial r}(1,\theta) = k_2\frac{\partial T_2}{\partial r}(1,\theta), \quad \theta\in[\pi/2,\pi]. \end{aligned} \tag{23}$$

The difference of the tangential stresses is balanced by the surface gradient of the interfacial tension

$$\Pi_{r\theta,1}(1,\theta) - \mu_2\Pi_{r\theta,2}(1,\theta) = \frac{\partial T_1}{\partial\theta}(1,\theta), \tag{24}$$

where $\Pi_{r\theta,i} = r\frac{\partial}{\partial r}(\frac{v_{\theta,i}}{r}) + \frac{1}{r}\frac{\partial v_{r,i}}{\partial\theta}$.

In order to solve the equations Eq. 17 with the boundary conditions Eqs. 20–24, we make asymptotic expansions for the velocity (the streamfunction) and temperature fields outside and inside the droplet with the small perturbation

Fig. 6 (continued)

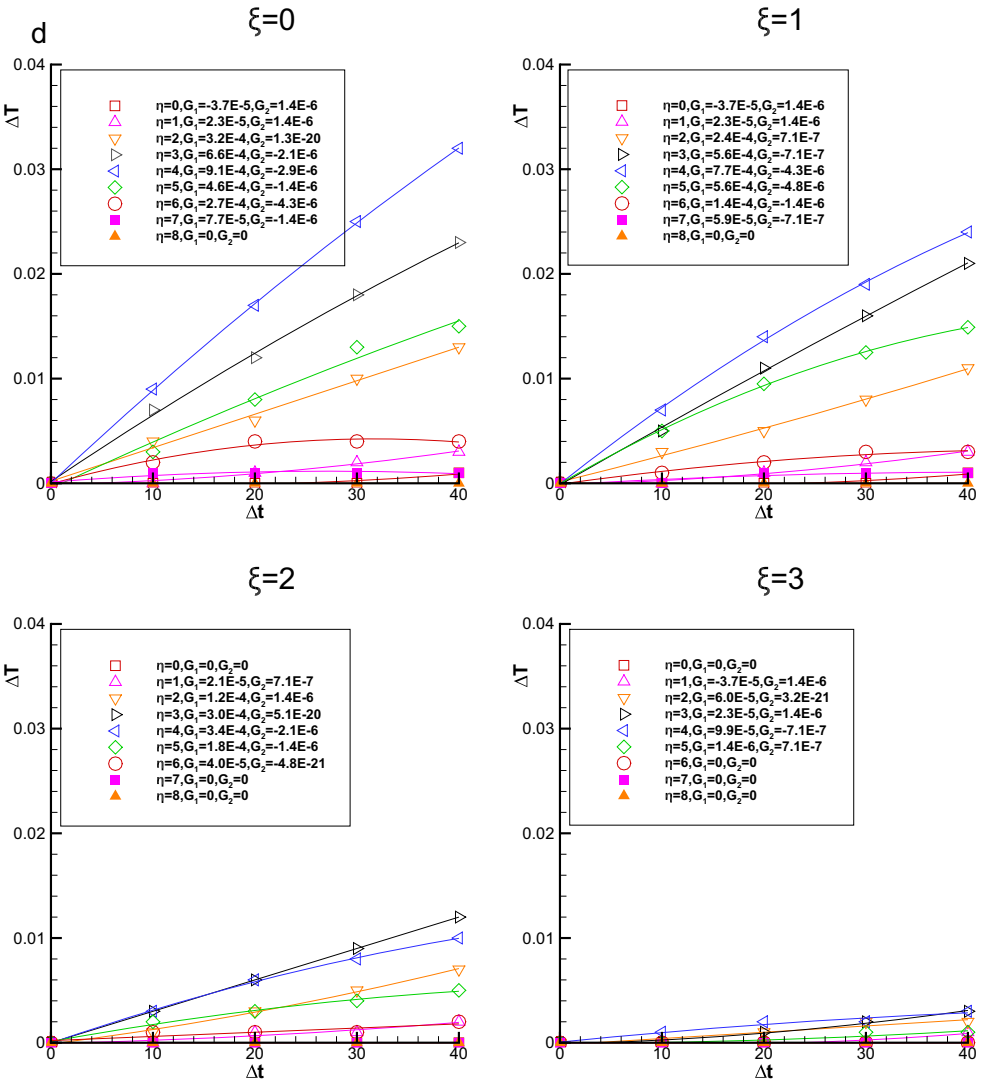

parameter Re as follows

$$\begin{aligned}
\psi_i(r,\theta) &= \psi_i^0(r,\theta) + Re\psi_i^1(r,\theta) + o(Re),\\
T_i(r,\theta) &= T_i^0(r,\theta) + ReT_i^1(r,\theta) + o(Re),\\
V_\infty &= V_\infty^0 + ReV_\infty^1 + o(Re).
\end{aligned} \tag{25}$$

Using the series expansions Eq. 25, we can obtain governing equations of the leading-order streamfunctions (ψ_i^0) and temperatures (T_i^0) derived from the momentum and the energy equations Eq. 17 as

$$\begin{aligned}
E^4\psi_i^0 &= 0,\\
\Delta T_i^0 &= 0.
\end{aligned} \tag{26}$$

Following the derivations (Oliver and Dewitt 1988), the solutions of the governing Eq. 26 satisfying the boundary conditions Eqs. 20–24 described by the leading-order ψ_i^0 and T_i^0 are written as

$$\begin{aligned}
\psi_1^0 &= \frac{V_\infty^0}{2}(r^2 - r^{-1})\sin^2\theta\\
&\quad + \sum_{n=3,odd}^{\infty} D_n(r^{3-n} - r^{1-n})C_n^{-1/2}(\cos\theta),\\
\psi_2^0 &= \frac{3V_\infty^0}{4}(r^4 - r^2)\sin^2\theta\\
&\quad + \sum_{n=3,odd}^{\infty} D_n(r^{2+n} - r^n)C_n^{-1/2}(\cos\theta)
\end{aligned} \tag{27}$$

and

$$\begin{aligned}
T_1^0 &= \frac{1}{4r} + \frac{1}{2(2+k_2)}r^{-2}\cos\theta\\
&\quad + \sum_{n=2,even}^{\infty} a_n r^{-(n+1)} P_n(\cos\theta),\\
T_2^0 &= \frac{1}{4} + \frac{1}{2(2+k_2)}r\cos\theta\\
&\quad + \sum_{n=2,even}^{\infty} a_n r^n P_n(\cos\theta),
\end{aligned} \tag{28}$$

where $a_n = (-1)^{(n-2)/2}\frac{2n+1}{2[(1+k_2)n+1](n+2)(n-1)}\Pi_{j=1}^{n/2}\frac{2j-1}{2j}$, $(n \geq 2, even)$, $D_n = \frac{n(n-1)}{2(2n-1)(1+\mu_2)}a_{n-1}$. $P_n(s)$ and $C_n^{-1/2}(s) = \int_s^1 P_{n-1}(x)dx$ are the Legendre and Gegenbauer polynomials of order n, respectively. The steady migration velocity is obtained through the leading-order net force balance condition and written as

$$V_\infty^0 = \frac{1}{3(2+3\mu_2)(2+k_2)}. \tag{29}$$

Substituting the expansions Eq. 25 into the momentum and the energy equations Eq. 17, we obtain the governing equations of the first-order streamfunctions (ψ_i^1) and temperatures (T_i^1) of the two-phase fluids

$$\begin{aligned}
&\frac{\mu_i}{\rho_i}E^4\psi_i^1 = \frac{1}{r^2}\frac{\partial(\psi_i^0, E^2\psi_i^0)}{\partial(r,\cos\theta)} + \frac{2}{r^2}E^2\psi_i^0 L\psi_i^0,\\
&\Delta T_i^1 = 0.
\end{aligned} \tag{30}$$

The streamfunctions ψ_i^1 and the temperatures T_i^1 should satisfy the boundary conditions at infinity

$$\begin{aligned}
&\mathbf{v}_1^1(r\to\infty,\theta) \to (-V_\infty^1\cos\theta, V_\infty^1\sin\theta),\\
&T_1^1(r\to\infty,\theta)\to 0
\end{aligned} \tag{31}$$

and at interface

$$\begin{aligned}
&v_{r,1}^1(1,\theta) = v_{r,2}^1(1,\theta) = 0,\\
&v_{\theta,1}^1(1,\theta) = v_{\theta,2}^1(1,\theta),\\
&T_1^1(1,\theta) = T_2^1(1,\theta),\\
&\frac{\partial T_1^1}{\partial r}(1,\theta) = k_2\frac{\partial T_2^1}{\partial r}(1,\theta),\\
&\Pi_{r\theta,1}^1(1,\theta) - \mu_2\Pi_{r\theta,2}^1(1,\theta) = \frac{\partial T_1^1}{\partial\theta}(1,\theta).
\end{aligned} \tag{32}$$

In order to obtain simplified analytical solutions (ψ_i^1, T_i^1) of the above equations, we truncate the leading-order streamfunctions ψ_i^0 and the leading-order temperature T_i^0 at $n = 3$ in Eqs. 27, 28 and write, respectively, as

$$\begin{aligned}
\psi_1^0 &= \frac{V_\infty^0}{2}(r^2 - r^{-1})\sin^2\theta\\
&\quad + \frac{3a_2}{5(1+\mu_2)}(1-r^{-2})C_3^{-1/2}(\cos\theta),\\
\psi_2^0 &= \frac{3V_\infty^0}{4}(r^4 - r^2)\sin^2\theta\\
&\quad + \frac{3a_2}{5(1+\mu_2)}(r^5 - r^3)C_3^{-1/2}(\cos\theta),
\end{aligned} \tag{33}$$

and

$$\begin{aligned}
T_1^0 &= \frac{1}{4r} + \frac{1}{2(2+k_2)}r^{-2}\cos\theta + a_2 r^{-3}P_2(\cos\theta),\\
T_2^0 &= \frac{1}{4} + \frac{1}{2(2+k_2)}r\cos\theta + a_2 r^2 P_2(\cos\theta),
\end{aligned} \tag{34}$$

where $a_2 = \frac{5}{8(3+2k_2)}$. As shown in Fig. 7, the velocity and the temperature fields based on (ψ_i^0, T_i^0) truncated at $n = 3$ and 5 in Eqs. 27, 28 are similar each other. The truncated streamfunctions ψ_i^0 at $n = 3$ can be thought as a reasonable approximation of the leading-order streamfunctions. By using the truncated streamfunctions ψ_i^0, the solutions of Eq. 30 satisfying the boundary conditions Eqs. 31 - 32 are determined as

$$\begin{aligned}
\psi_1^1 &= -\frac{a_2}{1+\mu_2}V_\infty^0\left[\frac{3}{25}r + \frac{3}{20}r^{-2}\right]C_4^{-1/2}(\cos\theta)\\
&\quad - \frac{a_2^2}{(1+\mu_2)^2}r^{-3}\left[\frac{27}{350}C_5^{-1/2}(\cos\theta)\right.\\
&\quad \left. + \frac{1}{350}C_3^{-1/2}(\cos\theta) + \frac{27}{14000}C_1^{-1/2}(\cos\theta)\right]\\
&\quad + V_\infty^1 r^2 C_2^{-1/2}(\cos\theta) + (b_1 + d_1 r)C_1^{-1/2}(\cos\theta) + b_0 r\\
&\quad + \sum_{n=2}^{5}(b_n r^{1-n} - d_n r^{3-n})C_n^{-1/2}(\cos\theta),\\
\psi_2^1 &= -\frac{\rho_2}{\mu_2}\left\{\frac{5}{28}(V_\infty^0)^2 r^7 C_3^{-1/2}(\cos\theta)\right.\\
&\quad + \frac{a_2^2}{(1+\mu_2)^2}\left[\frac{9}{715}r^9 C_5^{-1/2}(\cos\theta)\right.\\
&\quad \left.\left. + \left(\frac{1}{220}r^9 - \frac{1}{100}r^7\right)C_3^{-1/2}(\cos\theta)\right]\right.\\
&\quad + \frac{a_2}{1+\mu_2}V_\infty^0\left[\frac{1}{10}r^8 C_4^{-1/2}(\cos\theta)\right.\\
&\quad + \left(\frac{13}{360}r^8 - \frac{107}{2100}r^6\right)C_2^{-1/2}(\cos\theta)\\
&\quad \left.\left. - \frac{1}{80}r^8 + \frac{107}{600}r^6\right]\right\} - \hat{d}_0 r^3\\
&\quad + \sum_{n=1}^{5}(\hat{b}_n r^n - \hat{d}_n r^{n+2})C_n^{-1/2}(\cos\theta)
\end{aligned} \tag{35}$$

and

$$\begin{aligned}
T_1^1 &= 0,\\
T_2^1 &= 0,
\end{aligned} \tag{36}$$

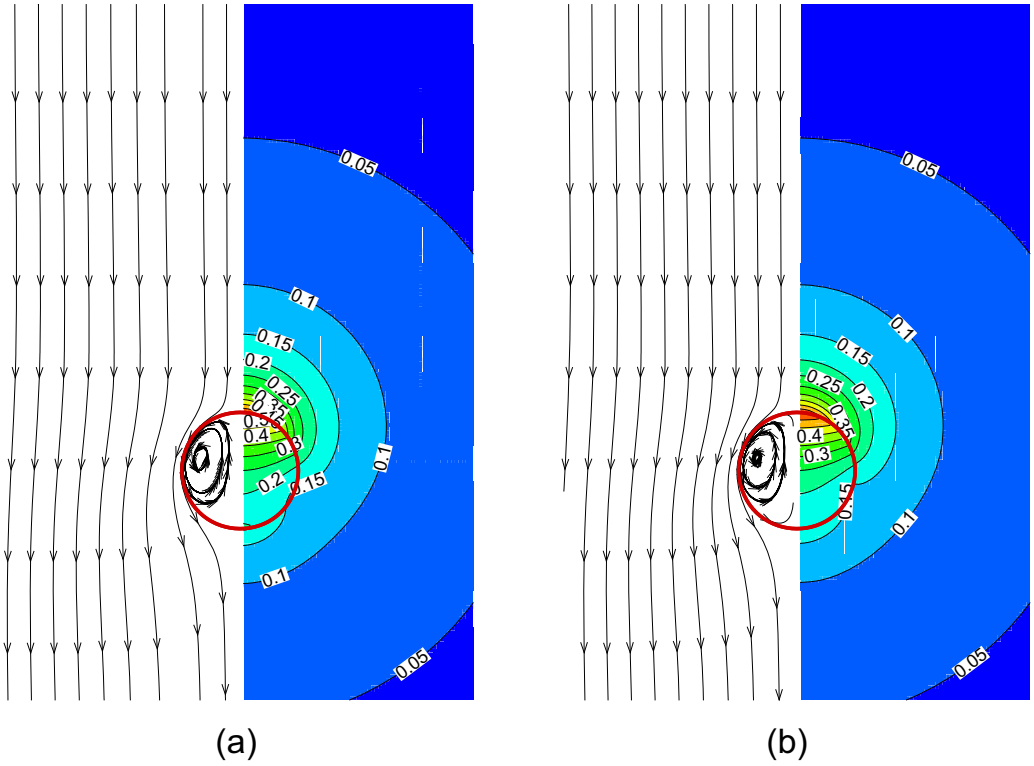

Fig. 7 Velocity and temperature fields truncated at **a** $n = 3$ and **b** $n = 5$ in Eqs. 27 and 28 for zero limits of Re and Ma numbers and $\rho_2 = \mu_2 = k_2 = \kappa_2 = 0.8$

where

$$
\begin{aligned}
b_0 &= \tfrac{271}{200}\tfrac{\rho_2 a_2}{1+\mu_2} V_\infty^0,\\
b_1 &= \left[\tfrac{\mu_2}{16(2+\mu_2)} - \tfrac{1}{1+2\mu_2}\right]\tfrac{27a_2^2}{875(1+\mu_2)^2},\\
b_2 &= \tfrac{6493}{11550}\tfrac{\rho_2 a_2}{(1+\mu_2)^2} V_{\infty,0} + \tfrac{\mu_2}{2(1+\mu_2)} V_\infty^1,\\
b_3 &= \left(\tfrac{9}{1735} - \tfrac{4\rho_2}{1375} + \tfrac{3\mu_2}{100}\right)\tfrac{a_2^2}{(1+\mu_2)^3} - \tfrac{6183}{20020}\tfrac{\rho_2}{1+\mu_2}(V_\infty^0)^2,\\
b_4 &= \left(\tfrac{27}{5500} - \tfrac{9\mu_2}{20}\right)\tfrac{a_2}{(1+\mu_2)^2} V_\infty^0,\\
b_5 &= \left(\tfrac{27}{1330} + \tfrac{54\rho_2}{13585} + \tfrac{27\mu_2}{700}\right)\tfrac{a_2^2}{(1+\mu_2)^3},\\
d_1 &= b_1 - \tfrac{27}{14000}\tfrac{a_2^2}{(1+\mu_2)^2},\\
d_2 &= b_2 + V_\infty^1,\\
d_3 &= b_3 - \tfrac{1}{350}\tfrac{a_2^2}{(1+\mu_2)^2},\\
d_4 &= b_4 - \tfrac{27}{100}\tfrac{a_2}{1+\mu_2} V_\infty^0,\\
d_5 &= b_5 - \tfrac{27}{350}\tfrac{a_2^2}{(1+\mu_2)^2}
\end{aligned}
\tag{37}
$$

and

$$
\begin{aligned}
\hat{b}_1 &= \tfrac{1}{2} b_1 - \tfrac{27}{14000}\tfrac{a_2^2}{(1+\mu_2)^2},\\
\hat{b}_2 &= b_2 - \tfrac{67}{3150}\tfrac{\rho_2}{\mu_2}\tfrac{a^2}{1+\mu_2} V_\infty^0 - \tfrac{1}{2} V_\infty^1,\\
\hat{b}_3 &= b_3 - \left(\tfrac{3}{700} - \tfrac{1}{1100}\tfrac{\rho_2}{\mu_2}\right)\tfrac{a_2^2}{(1+\mu_2)^2} - \tfrac{9}{715}\tfrac{\rho_2}{\mu_2}(V_\infty^0)^2,\\
\hat{b}_4 &= b_4 + \left(\tfrac{9}{20} - \tfrac{1}{10}\tfrac{\rho_2}{\mu_2}\right)\tfrac{a_2}{1+\mu_2} V_\infty^0,\\
\hat{b}_5 &= b_5 - \left(\tfrac{27}{700} + \tfrac{9}{715}\tfrac{\rho_2}{\mu_2}\right)\tfrac{a_2^2}{(1+\mu_2)^2},\\
\hat{d}_0 &= -\tfrac{1}{3} b_0 - \tfrac{97}{300}\tfrac{\rho_2 a_2}{\mu_2(1+\mu_2)} V_\infty^0,\\
\hat{d}_1 &= \hat{b}_1,\\
\hat{d}_2 &= \hat{b}_2 + \tfrac{187}{12600}\tfrac{\rho_2 a_2}{\mu_2(1+\mu_2)} V_\infty^0,\\
\hat{d}_3 &= \hat{b}_3 + \tfrac{3}{550}\tfrac{\rho_2 a_2^2}{\mu_2(1+\mu_2)^2} - \tfrac{5}{28}\tfrac{\rho_2}{\mu_2}(V_\infty^0)^2,\\
\hat{d}_4 &= \hat{b}_4 - \tfrac{1}{10}\tfrac{\rho_2 a_2}{\mu_2(1+\mu_2)} V_\infty^0,\\
\hat{d}_5 &= \hat{b}_5 - \tfrac{9}{715}\tfrac{\rho_2 a_2^2}{\mu_2(1+\mu_2)^2}.
\end{aligned}
\tag{38}
$$

Setting the first-order net force on the droplet in the vertical direction to zero, we have

$$
F_z^1 = \int_0^\pi (\Pi_{rr,1}^1 \cos\theta - \Pi_{r\theta,1}^1 \sin\theta)|_1 \sin\theta d\theta = 0, \tag{39}
$$

where

$$
\Pi_{rr,1}^1 = -p_1^1 + 2\frac{\partial v_{r,1}^1}{\partial r}. \tag{40}
$$

Integrating the momentum equation of continuous phase fluid in Eq. 16, we obtain the first-order pressure field outside the droplet as

$$\begin{aligned} p_1^1(r,\theta) = {} & (V_\infty^0)^2 r^{-3}\left[\left(1-\tfrac{5}{12}r^{-3}\right)P_2(\cos\theta)-\tfrac{1}{12}r^{-3}\right] \\ & +\tfrac{V_\infty^0 a_2}{1+\mu_2}r^{-2}\left[\left(\tfrac{144}{75}+\tfrac{3}{25}r^{-2}+\tfrac{153}{250}r^{-3}-\tfrac{12}{25}r^{-5}\right]\right. \\ & P_3(\cos\theta) \\ & \left.-\left(\tfrac{3}{5}-\tfrac{21}{125}r^{-3}+\tfrac{3}{25}r^{-5}\right)P_1(\cos\theta)\right] \\ & -\tfrac{a_2^2}{(1+\mu)^2}r^{-3}\left[\left(\tfrac{81}{875}-\tfrac{236}{875}r^{-3}+\tfrac{9}{175}r^{-5}\right)\right. \\ & P_4(\cos\theta) \\ & -\left(\tfrac{9}{175}+\tfrac{3}{70}r^{-3}-\tfrac{3}{35}r^{-5}\right)P_2(\cos\theta) \\ & \left.+\left(\tfrac{27}{1750}-\tfrac{417}{3500}r^{-3}+\tfrac{39}{350}r^{-5}\right)\right] \\ & -\textstyle\sum_{n=2}^{5}\tfrac{6-4n}{n}d_n r^{-n}P_{n-1}(\cos\theta). \end{aligned} \tag{41}$$

Substituting the solutions Eqs. 35 and 41 into 39, we can determine

$$\begin{aligned} V_\infty^1 &= -\left(\tfrac{3}{125}+\tfrac{6493}{5775}\tfrac{\rho_2}{2+3\mu_2}\right)\tfrac{a_2}{1+\mu_2}V_\infty^0 \\ &= -\tfrac{1}{8}\left(\tfrac{3}{25}+5\tfrac{718}{1155}\tfrac{\rho_2}{2+3\mu_2}\right)\tfrac{1}{(1+\mu_2)(3+2k_2)}V_\infty^0. \end{aligned} \tag{42}$$

The steady migration velocity of the droplet is thus expressed as

$$\begin{aligned} V_\infty &= V_\infty^0 + Re\,V_\infty^1 + o(Re) \\ &= V_\infty^0\left[1-Re\tfrac{1}{8}\left(\tfrac{3}{25}+5\tfrac{718}{1155}\tfrac{\rho_2}{2+3\mu_2}\right)\tfrac{1}{(1+\mu_2)(3+2k_2)}\right]+o(Re). \end{aligned} \tag{43}$$

It is noted that the steady thermocapillary migration speed of the droplet decreases as Re number increases. In comparison with the leading-order migration velocity V_∞^0, the first-order migration velocity V_∞^1 depends on the density ratio of two-phase fluids, except on the viscosity and the thermal conductivity ratios of the two-phase fluids. Figure 8 displays the comparison between the above analytical result Eq. 43 on the steady droplet migration velocity versus small Re number at the zero limit of Ma number with the corresponding numerical result at Ma=0.01 in a range of small Re numbers, where $\rho_2 = \mu_2 = k_2 = \kappa_2 = 0.8$. The numerical result is in qualitatively agreement with the analytical profile, although the former absolute slope is slight smaller than the later one.

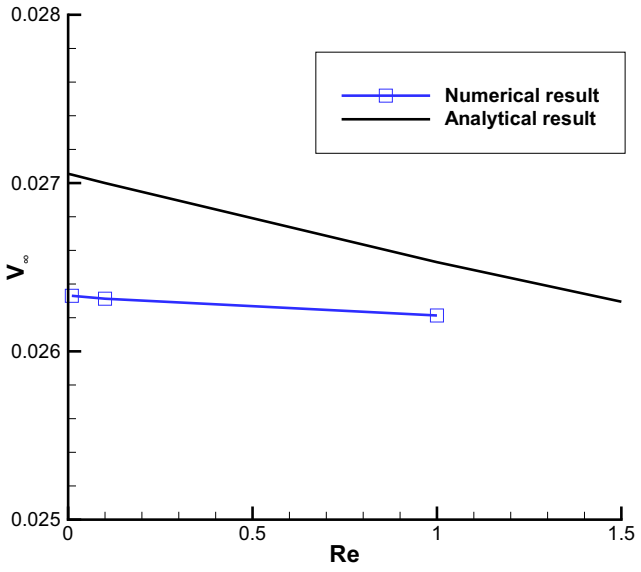

Fig. 8 Comparison of the analytical result Eq. 43 on the steady droplet migration velocity V_∞ versus small Re number at the zero limit of Ma number with the corresponding numerical result at Ma=0.01 in a range of small Re numbers, where $\rho_2 = \mu_2 = k_2 = \kappa_2 = 0.8$

Conclusion and discussion

In this paper, under thermal radiation with a uniform flux, thermocapillary migration of a droplet is numerically investigated and theoretically analyzed. By using the front-tracking method, it is observed that thermocapillary droplet migration at small Re numbers and moderate Ma numbers can reach a steady process. The steady migration velocity decreases as Ma number increases. In the steady migration process, the non-separated external flow around the droplet and the internal vortex flow appear inside the droplet. In the temperature fields, the internal and external isotherms intersect with the surface of the droplet and form a mushroom-cape or an umbrella shape. The former characteristics is similar to that in thermocapillary droplet migration with a vertical temperature gradient, while the later is different. It is found that the temperature fields in the steady migration process undergo a quadratic function increasing process with relative time. In the steady droplet migration process, where the nonlinear term in the quadratic function is one or more orders of magnitude lower than the linear term, the linear rise of the steady state temperatures with the relative time is a main characteristics.

The steady energy equations are derived based on the assumption of the quadratic function time-evolution of the temperature fields. From the steady momentum and energy equations, an analytical result at small Re number and zero Ma number is determined by using the method of matched asymptotic expansions. The steady migration velocity of the droplet, which depends on the density, the viscosity and the thermal conductivity ratios of the two-phase fluids, decreases as Re number increases. The analytical result is in qualitatively agreement with the numerical one.

We emphasize that all of the above results pertain to the highly idealized axisymmetric model with the gray droplet and the transparent continuous-phase fluid to the radiation, and show the effects of Ma number on the terminal velocity and the time evolution of temperature fields in the steady state migration processes. The motivation of the current

work is very different from the ZLCXS' one for the effects of Re number on the terminal velocity (Zhang et al. 2018). Whether the properties of the steady state temperature fields in the simple model can refer to or be extended to the more realistic models remains to be determined.

Acknowledgments This research is supported by the National Natural Science Foundation of China through Grants No. 11172310 and No. 11472284 and the CAS Strategic Priority Research Program XDB22040403. The author thanks the Institute of Mechanics of CAS research computing facility for assisting in the computation.

Appendix: Steady continuity, momentum and energy equations derived from the laboratory coordinate system

Using the coordinate and variable transformations from the laboratory coordinate system $(\bar{r}, \bar{z})$ to a coordinate system (r, z) moving with the droplet velocity V_∞ described below

$$\bar{\mathbf{r}} = \mathbf{r} + V_\infty(t - t_s)\mathbf{i}_z \tag{A.1}$$

and

$$\begin{aligned}
&\bar{\mathbf{v}}_i(\bar{\mathbf{r}}, t) = \mathbf{v}_i(\mathbf{r}) + V_\infty \mathbf{i}_z,\\
&\bar{p}_i(\bar{\mathbf{r}}, t) = p_i(\mathbf{r}),\\
&\bar{T}_i(\bar{\mathbf{r}}, t) = T_i(\mathbf{r}) + G_1(\mathbf{r})(t - t_s) + G_2(\mathbf{r})(t - t_s)^2,
\end{aligned} \tag{A.2}$$

we have

$$\begin{aligned}
\bar{\nabla}|_t &= \left.\frac{\partial}{\partial \bar{r}}\right|_t \mathbf{i}_r + \left.\frac{\partial}{\partial \bar{z}}\right|_t \mathbf{i}_z = \left.\frac{\partial}{\partial r}\right|_t \mathbf{i}_r + \left.\frac{\partial}{\partial z}\right|_t \mathbf{i}_z = \nabla|_t,\\
\bar{\Delta}|_t &= \left.\frac{\partial^2}{\partial \bar{r}^2}\right|_t + \left.\frac{\partial^2}{\partial \bar{z}^2}\right|_t = \left.\frac{\partial^2}{\partial r^2}\right|_t + \left.\frac{\partial^2}{\partial z^2}\right|_t = \Delta|_t.
\end{aligned} \tag{A.3}$$

where $\mathbf{v}_i(\mathbf{r})$, $p_i(\mathbf{r})$ and $T_i(\mathbf{r})$ are the velocity, pressure, temperature fields in the coordinate system (r, z) moving with the droplet velocity V_∞ when the steady migration process holds at the time $t \geq t_s$. For the continuous equations of the two-phase fluids in Eq. 5, we can directly obtain the steady continuous equations

$$\bar{\nabla} \cdot \bar{\mathbf{v}}_i = \bar{\nabla} \cdot (\mathbf{v}_i + V_\infty \mathbf{i}_z) = \nabla \cdot \mathbf{v}_i = 0. \tag{A.4}$$

For the momentum equations of the two-phase fluid in Eq. 5, we derive their unsteady, convection, pressure gradient and viscous terms as follows

$$\begin{aligned}
\left.\frac{\partial \bar{\mathbf{v}}_i}{\partial t}\right|_{\bar{\mathbf{r}}} &= \left.\frac{\partial(\mathbf{v}_i + V_\infty \mathbf{i}_z)}{\partial t}\right|_{\bar{\mathbf{r}}} = \left.\frac{\partial \mathbf{v}_i}{\partial t}\right|_{\bar{\mathbf{r}}} = \left.\frac{\partial \mathbf{v}_i}{\partial r}\right|_t \left.\frac{\partial r}{\partial t}\right|_{\bar{\mathbf{r}}}\\
&\quad + \left.\frac{\partial \mathbf{v}_i}{\partial z}\right|_t \left.\frac{\partial z}{\partial t}\right|_{\bar{\mathbf{r}}} + \left.\frac{\partial \mathbf{v}_i}{\partial t}\right|_{\mathbf{r}} \left.\frac{\partial t}{\partial t}\right|_{\bar{\mathbf{r}}}\\
&= \cdot \left.\frac{\partial \mathbf{v}_i}{\partial z}\right|_t (-V_\infty) + \left.\frac{\partial \mathbf{v}_i}{\partial t}\right|_{\mathbf{r}} = -V_\infty \frac{\partial \mathbf{v}_i}{\partial z},\\
\bar{\mathbf{v}}_i \cdot \bar{\nabla}\bar{\mathbf{v}}_i|_t &= (\mathbf{v}_i + V_\infty \mathbf{i}_z) \cdot \bar{\nabla}(\mathbf{v}_i + V_\infty \mathbf{i}_z)|_t\\
&= (\mathbf{v}_i + V_\infty \mathbf{i}_z) \cdot \bar{\nabla}\mathbf{v}_i|_t\\
&= \mathbf{v}_i \cdot \nabla \mathbf{v}_i + V_\infty \frac{\partial \mathbf{v}_i}{\partial z},\\
\bar{\nabla}\bar{p}_i|_t &= \bar{\nabla} p_i|_t = \nabla p_i,\\
\bar{\Delta}\bar{\mathbf{v}}_i|_t &= \bar{\Delta}(\mathbf{v}_i + V_\infty \mathbf{i}_z)|_t = \bar{\Delta}\mathbf{v}_i|_t = \Delta \mathbf{v}_i,
\end{aligned} \tag{A.5}$$

where $\frac{\partial r}{\partial t}|_{\bar{\mathbf{r}}} = \frac{\partial r}{\partial t}|_{\bar{r}} = 0$, $\frac{\partial z}{\partial t}|_{\bar{\mathbf{r}}} = \frac{\partial z}{\partial t}|_{\bar{z}} = -V_\infty$ and $\frac{\partial \mathbf{v}_i}{\partial t}|_{\mathbf{r}} = 0$. Substituting Eq. A.5 into the second equation in Eq. 5, we can obtain the steady momentum equations

$$\rho_i \mathbf{v}_i \cdot \nabla \mathbf{v}_i = -\nabla p_i + \frac{\mu_i}{Re} \Delta \mathbf{v}_i. \tag{A.6}$$

And for energy equations of the two-phase fluids in Eq. 5, we can write their unsteady, convection and conductivity terms as follows

$$\begin{aligned}
\left.\frac{\partial \bar{T}_i}{\partial t}\right|_{\bar{\mathbf{r}}} &= \left.\frac{\partial T_i}{\partial t}\right|_{\bar{\mathbf{r}}} + \left.\frac{\partial G_1}{\partial t}\right|_{\bar{\mathbf{r}}} (t - t_s) + G_1\\
&\quad + \left.\frac{\partial G_2}{\partial t}\right|_{\bar{\mathbf{r}}} (t - t_s)^2 + 2G_2(t - t_s)\\
&= \left.\frac{\partial T_i}{\partial r}\right|_t \left.\frac{\partial r}{\partial t}\right|_{\bar{\mathbf{r}}} + \left.\frac{\partial T_i}{\partial z}\right|_t \left.\frac{\partial z}{\partial t}\right|_{\bar{\mathbf{r}}} + \left.\frac{\partial T_i}{\partial t}\right|_{\mathbf{r}} \left.\frac{\partial t}{\partial t}\right|_{\bar{\mathbf{r}}}\\
&\quad + \left.\frac{\partial G_1}{\partial r}\right|_t \left.\frac{\partial r}{\partial t}\right|_{\bar{\mathbf{r}}} (t - t_s) + \left.\frac{\partial G_1}{\partial z}\right|_t \left.\frac{\partial z}{\partial t}\right|_{\bar{\mathbf{r}}} (t - t_s)\\
&\quad + \left.\frac{\partial G_1}{\partial t}\right|_{\mathbf{r}} \left.\frac{\partial t}{\partial t}\right|_{\bar{\mathbf{r}}} (t - t_s) + G_1\\
&\quad + \left.\frac{\partial G_2}{\partial r}\right|_t \left.\frac{\partial r}{\partial t}\right|_{\bar{\mathbf{r}}} (t - t_s)^2 + \left.\frac{\partial G_2}{\partial z}\right|_t \left.\frac{\partial z}{\partial t}\right|_{\bar{\mathbf{r}}} (t - t_s)^2\\
&\quad + \left.\frac{\partial G_2}{\partial t}\right|_{\mathbf{r}} \left.\frac{\partial t}{\partial t}\right|_{\bar{\mathbf{r}}} (t - t_s)^2 + 2G_2(t - t_s)\\
&= \left.\frac{\partial T_i}{\partial z}\right|_t (-V_\infty) + \left.\frac{\partial T_i}{\partial t}\right|_{\mathbf{r}}\\
&\quad + \left.\frac{\partial G_1}{\partial z}\right|_t (-V_\infty)(t - t_s) + \left.\frac{\partial G_1}{\partial t}\right|_{\mathbf{r}} (t - t_s) + G_1\\
&\quad + \left.\frac{\partial G_2}{\partial z}\right|_t (-V_\infty)(t - t_s)^2 + \left.\frac{\partial G_2}{\partial t}\right|_{\mathbf{r}} (t - t_s)^2\\
&\quad + 2G_2(t - t_s)
\end{aligned}$$

$$
\begin{aligned}
&= -V_\infty \frac{\partial T_i}{\partial z} - V_\infty \frac{\partial G_1}{\partial z}(t-t_s) + G_1 \\
&\quad -V_\infty \frac{\partial G_2}{\partial z}(t-t_s)^2 + 2G_2(t-t_s), \\
\bar{\mathbf{v}}_i \cdot \bar{\nabla}\bar{T}_i\big|_t &= (\mathbf{v}_i + V_\infty \mathbf{i}_z) \cdot \bar{\nabla}(T_i + G_1(t-t_s) \\
&\quad +G_2(t-t_s)^2)\Big|_t \\
&= (\mathbf{v}_i + V_\infty \mathbf{i}_z) \cdot (\bar{\nabla} T_i|_t + \bar{\nabla} G_1|_t (t-t_s) \\
&\quad +\bar{\nabla} G_2|_t (t-t_s)^2) \\
&= \mathbf{v}_i \cdot \nabla T_i + V_\infty \frac{\partial T_i}{\partial z} + \mathbf{v}_i \cdot \nabla G_1 (t-t_s) \\
&\quad +V_\infty \frac{\partial G_1}{\partial z}(t-t_s) \\
&\quad +\mathbf{v}_i \cdot \nabla G_2 (t-t_s)^2 + V_\infty \frac{\partial G_2}{\partial z}(t-t_s)^2, \\
\bar{\Delta}\bar{T}_i|_t &= \bar{\Delta}(T_i + G_1(t-t_s) + G_2(t-t_s)^2)|_t \\
&= \bar{\Delta} T_i|_t + \bar{\Delta} G_1|_t (t-t_s) + \bar{\Delta} G_2|_t (t-t_s)^2 \\
&= \Delta T_i + \Delta G_1 (t-t_s) + \Delta G_2 (t-t_s)^2, \qquad \text{(A.7)}
\end{aligned}
$$

where $\frac{\partial T_i}{\partial t}|_{\mathbf{r}} = \frac{\partial G_1}{\partial t}|_{\mathbf{r}} = \frac{\partial G_2}{\partial t}|_{\mathbf{r}} = 0$. Substituting Eq. A.7 into the third equation in Eq. 5, we can derive the energy equations as follows

$$
\begin{aligned}
&G_1 + \mathbf{v}_i \cdot \nabla T_i - \frac{\kappa_i}{Ma}\Delta T_i \\
&= -[(\mathbf{v}_i \cdot \nabla G_1) - \frac{\kappa_i}{Ma}\Delta G_1 + 2G_2](t-t_s) \\
&\quad -[(\mathbf{v}_i \cdot \nabla G_2) - \frac{\kappa_i}{Ma}\Delta G_2](t-t_s)^2. \qquad \text{(A.8)}
\end{aligned}
$$

Since the left-hand terms are independent of time and the right-hand terms are a quadratic function of the relative time, the steady energy equations can be derived as

$$
\begin{aligned}
&G_1 + \mathbf{v}_i \cdot \nabla T_i - \frac{\kappa_i}{Ma}\Delta T_i = 0, \\
&\mathbf{v}_i \cdot \nabla G_1 - \frac{\kappa_i}{Ma}\Delta G_1 + 2G_2 = 0, \\
&\mathbf{v}_i \cdot \nabla G_2 - \frac{\kappa_i}{Ma}\Delta G_2 = 0. \qquad \text{(A.9)}
\end{aligned}
$$

References

Alhendal, Y., Turan, A., Kalendar, A., Abou-Ziyan, H., Ei-shiaty, R.: Thermocapillary bubbker migration at high reynolds and marangoni numbers:3D numerical studt. Microgravity Sci Technol. **30**, 561 (2018)

Baroud, C.N., Delville, J.P., Gallaire, F., Wunenburger, R.: Thermocapillary value for droplet production and sorting. Phys. Rev. E **75**, 046302 (2007)

Bassano, E., Castagnolo, D.: Marangoni migration of a methanol drop in cyclohexane matrix in a closed cavity. Microgravity Sci Technol. **14**, 20 (2003)

Lopez, P., Ryzantsev, Y.S., Rubio, R.G., Ortega, F., Velarde, M.G., Redondo, J.M.: Observation of the thermocapillary motion of a droplet in a laser beam. In: Rubio, R.G. et al. (eds.) Without Bounds: A Scientific Canvas of Nonlinearity and Complex Dynamics. Springer, Berlin (2013)

Oliver, D.L.R., Dewitt, K.J.: Surface tension driven flows for a droplet in a microgravity environment. Int. J. Heat Mass Trans. **31**, 1534 (1988)

Peskin, C.S.: Numerical analysis of blood flow in the heart. J. Comput. Phys. **25**, 220 (1977)

Ratke, L., Korekt, G.: Solidication of Al-Pb-Base alloys in low gravity. Z. Metallkde **91**, 919 (2000)

Rednikov, A.Y., Ryzzantsev, Y.S.: Thermocapillary motion of a droplet under the action of radiation. J. Appl. Mech. Tech. Phys. **30**, 337 (1989)

Rendondo, J.M., Lopez, P., Mahjoub, O.B., Ryazantsev, Y.S., Velarge, M.G.: Thermocapilariity and radiative heat flux oscillations. In: Topical Problems of Fluid Mechanics Prague (2014)

Ryazantsev, Y.S., Velarde, M.G., Rubio, R.G., Guzman, E., Ortega, F., Lopez, P.: Thermo- and soluto-capillarity: Passive and active drops. Adv. Coll. Interface Sci. **247**, 52 (2017)

Rybalko, S., Magome, N., Yoshikawa, K.: Forward and backward laser-guided motion of an oil droplet. Phys. Rev. E **70**, 046301 (2004)

Subramanian, R.S.: Slow migration of a gas bubble in a thermal gradient. AIChE J. **27**, 646 (1981)

Subramanian, R.S., Balasubramaniam, R., Wozniak, G.: Fluid mechanics of bubbles and drops. In: Monti, R. (ed.) Physics of Fluids in Microgravity,. Taylor & Francis, London (2001)

Tryggvason, G., Bunner, B., Esmaeeli, A., Juric, D., Al-Rawahi, N., tauber, W., Han, J., Nas, S., Jan, Y.: A front-tracking method for the computations of multiphase flow. J. Comput. Phys. **169**, 708 (2001)

Vincent, M.R., Delville, J.P.: Thermocapillary migration in small-scale temperature gradients: application to optofludic dispering. Phys. Rev. E **85**, 026310 (2012)

Wu, Z.-B.: Termical states of thermocapillary migration of a planar droplet at moderate and large Marangoni numbers. Int. J. Heat Mass Trans. **105**, 704 (2017)

Wu, Z.-B.: Steady thermocapillary migration of a droplet in a uniform temperature gradient combined with a radiation energy source at large Marangoni numbers. Phys. Rev. E **98**, 013110 (2018)

Wu, Z.-B., Hu, W.R.: Thermocapillary migration of a planar droplet at moderate and large Marangoni numbers. Acta Mech. **223**, 609 (2012)

Yin, Z., Wu, Z.-B., Hu, W.R.: Thermocapillary migration of drops and bubbles. In: Hu, W.R. (ed.) Advances in Microgravity Sciences. Transworld Research Network, Trivandrum (2009)

Young, N.O., Goldstein, J.S., Block, M.J.: The motion of bubbles in a vertical temperature gradient. J. Fluid Mech. **6**, 350 (1959)

Zhang, S., Duan, L., Kang, Q.: Experimental research on thermocapillary-buoyancy migration interaction of axissymetric two drops by using digital holographic interferometry. Microgravity Sci Technol. **30**, 183 (2018)

Zhang, B., Liu, D., Chen, Y., Xu, J., Sui, Y.: Numerical investigation on spontaneous droplet/bubble migration under thermal radiation. Int. J. Thermal Sci. **129**, 115 (2018)

Publisher's Note Springer Nature remains neutral with regard to jurisdictional claims in published maps and institutional affiliations.